



Science Arts & Métiers (SAM)

is an open access repository that collects the work of Arts et Métiers Institute of Technology researchers and makes it freely available over the web where possible.

This is an author-deposited version published in: <https://sam.ensam.eu>
Handle ID: [.http://hdl.handle.net/10985/19566](http://hdl.handle.net/10985/19566)

To cite this version :

X. XU, D.J. ALLEN, M.A.E. JEPSON, W. SUN, Adil BENAARBIA - Investigation of microstructural evolution and creep rupture behaviour of 9% Cr MarBN steel welds - Materials Science and Engineering: A - Vol. 791, p.139546 - 2020

Any correspondence concerning this service should be sent to the repository

Administrator : scienceouverte@ensam.eu



1 **Investigation of microstructural evolution and creep rupture**
2 **behaviour of 9% Cr MarBN steel welds**

3 X. Xu*¹, A. Benaarbia², D. Allen¹, Mark A. E. Jepson¹, W. Sun³

4 ¹Department of Materials, Loughborough University, Loughborough, Leicestershire
5 LE11 3TU, UK

6 ²Arts et Métiers, CNRS, Université de Lorraine, LEM3, F-57000 Metz, France

7 ³Department of Mechanical, Materials and Manufacturing Engineering, University of
8 Nottingham, Nottingham, Nottinghamshire, NG7 2RD, UK

9
10 **ABSTRACT**

11 The weldments made from the 9-12% Cr tempered martensitic steel are associated with
12 a complex microstructure arising from complicated thermal histories of the fusion and
13 heat affected zones. The complicated microstructural and micro-mechanical states in
14 these critical regions provide a challenge for the determination of creep failure
15 mechanisms. Based on detailed metallographic examination, the microstructural
16 distribution in the heat affected zone of the welds constructed using a recently developed
17 9% Cr MarBN steel, IBN-1, has been identified and classified into Equiaxed Zone (EZ),
18 Duplex Zone (DZ) and Over-tempered Zone (OZ). Cross-weld testing performed at
19 650°C has revealed a significant reduction in creep life as compared to bulk material.
20 Creep rupture has been shown to occur in the parent metal region with a ductile manner
21 at a high stress, whereas creep rupture initiates in the DZ region in an intergranular
22 manner at a low stress. Detailed metallographic investigation has further revealed a higher
23 damage susceptibility in the regions along the pre-existing Prior Austenite Grain
24 Boundaries (PAGBs). The diffusional reaustenitisation of local microstructure along the
25 PAGBs leads to a lower strength of matrix in combination with a lack of intergranular

26 precipitates as compared to the surrounding microstructure formed after displacive
27 reaustenitisation.

28 **KEYWORDS:** 9% Cr tempered martensitic steel; heat affected zone; multi-pass welding;
29 high temperature creep; failure mechanism

30 **1. INTRODUCTION**

31 The 9-12% Cr creep resistant martensitic steels are widely used in high temperature
32 pressure vessels and piping for the power generation industry due to their good
33 combination of creep strength and oxidation resistance. Based on a nominal composition
34 of Fe-9%Cr-3%W-3%Co-VNbBN [1], variants of Martensitic steel strengthened by
35 boron and nitrogen (MarBN) have been recently developed to replace the more
36 conventional 9% Cr materials such as the Grade 91 and 92 steels by providing superior
37 creep performance in combination with sufficient oxidation resistance [2]. During recent
38 years, the major developments based on the concept of MarBN include a range of
39 materials originating from international collaborative research activities including the
40 G115 (China), SAVE12AD (Japan), NPM-1 (Europe) and the IBN-1 (UK) steels [3–6].
41 These materials are typically manufactured by using common industrial processes
42 finished with normalisation and tempering to produce a tempered martensitic
43 microstructure in combination with secondary precipitates distributed both on grain
44 boundaries and within the grain interiors [1]. These MarBN steels are also compatible
45 with a variety of fusion welding processes including Manual Metal Arc Welding
46 (MMAW), Submerged Arc Welding (SAW) and Gas Tungsten Arc Weld (GTAW).
47 Multi-pass welding processes have been used to fabricate welds on MarBN steels to
48 achieve sufficient ductility in the weld metal and the Heat Affected Zone (HAZ).

49 Interest in the creep performance of welds fabricated in 9-12% Cr steels is increasing due
50 to their potential applications in power plant systems. The evaluation of welded joint
51 behaviour during creep exposure is a key factor in determining the lifetime of power plant
52 components. The existing studies of cross-weld samples under creep conditions have
53 shown that the ratio of creep rupture strength between cross-welds and the parent material
54 depends on both creep loading conditions and welding procedure [7]. At low testing
55 temperatures there is no large difference between parent metal and cross-weld creep
56 strength, whilst this difference becomes important at high temperatures and low stress
57 levels. Additionally, rupture locations were found to shift from the weld metal to the HAZ
58 as the applied stress decreased [8]. No substantial differences were found in the minimum
59 creep rate, the time to fracture and creep ductility for the cross-weld specimens taken
60 from different locations of the weld [8].

61 The welds fabricated in 9-12% Cr steels are associated with premature creep failure
62 within the HAZ, typically termed as 'Type IV' failure [9]. Type IV failure is commonly
63 presented in the HAZ region close to the boundary with the parent metal and causes a
64 substantial loss in creep strength for weldments as compared to bulk materials [10,11].
65 Detailed metallographic examination conducted on interrupted creep test specimens has
66 revealed the presence of creep cavities prior to final rupture in a Type IV manner [12].
67 Based on extensive metallographic examination, the metallurgical cause for the formation
68 of creep cavities is complicated and linked with a range of factors relating to the
69 microstructure of 9-12% Cr steels. For instance, the presence of second phase particles
70 (e.g. boron nitride, BN) above a critical size has been determined as a critical issue that
71 promotes the formation of cavities from the early stage of creep [12,13]. The presence of
72 Type IV failure in 9-12% Cr steels is also related with a layer of HAZ material exhibiting

73 a refined martensitic microstructure in combination with a lack of precipitate formation
74 on lath and grain boundaries [14,15]. However, most of the existing studies are conducted
75 using welds made from conventional materials such as Grade 91 and 92 steels, whilst the
76 research focused on the creep failure mechanism of recently developed MarBN steels is
77 comparatively limited.

78 Detailed investigation of the creep failure mechanism of 9-12% Cr steel welds is also
79 challenging due to a complicated HAZ microstructure formed by the complex thermal
80 distribution established during multi-pass welding. Extensive research has been
81 conducted using experimental measurement and numerical modelling techniques to
82 understand the thermal distribution in the HAZ [16–18]. These studies reveal that the
83 thermal history of the HAZ is typically composed of a heating phase with a heating rate
84 of $>100^{\circ}\text{C/s}$ and a subsequent cooling phase during which temperature decreases to the
85 ambient level within tens of seconds [16,17]. The variation of the microstructure in the
86 HAZ has been further correlated with thermal distribution based on detailed
87 metallographic examination and dilatometry simulation in 9-12% Cr steels as reported in
88 [19,20]. Detailed previous studies conducted on a more conventional Grade 92 alloy have
89 classified the HAZ microstructure into three critical sub-regions: Completely
90 Transformed Zone (CTZ), Partially Transformed Zone (PTZ) and Over-Tempered Zone
91 (OTZ) based on the range of peak temperatures reached during weld thermal cycles [20].
92 A more recent study based on the dilatometry simulation of a MarBN steel, IBN-1, has
93 further determined a similar trend of variation in the HAZ microstructure as a function of
94 peak temperature [21]. However, there is a lack of direct, systematic investigations from
95 the weld HAZs to correlate with the presence of creep damage in MarBN steels.

96 In the current research, the microstructural distribution in the HAZ of welds in a parent
 97 metal of the MarBN steel, IBN-1, has been investigated in detail in the initial state without
 98 creep exposure. The mechanical behaviour of the IBN-1 welds has been further
 99 investigated upon short-term creep exposure using cross-weld specimens at 650°C to
 100 compare with the bulk materials tested at similar testing conditions. Detailed
 101 metallographic examinations have been subsequently performed to identify the critical
 102 metallurgical factors related to the formation of creep damage after rupture at different
 103 stress levels.

104 **2. MATERIAL AND EXPERIMENTAL METHODS**

105 **2.1. Materials**

106 The chemical composition of the IBN-1 steel used (referred as parent metal) is listed in
 107 Table 1. The initial heat treatment of the parent metal involved a normalisation process
 108 at 1200°C for 4 hours and a tempering process at 765°C for 3 hours. A butt weld was then
 109 fabricated between the plates of parent metal that are ~30 mm in thickness by using a
 110 multi-pass MMAW process with a recently developed matching filler material, Metrode®
 111 Chromet® 933. In total, 26 weld beads were deposited with a heat input of 1.1 – 1.5 kJ/mm
 112 with the interpass temperature maintained between 200°C and 300°C. Post Weld Heat
 113 Treatment (PWHT) was conducted after welding at 760°C for 2 hours.

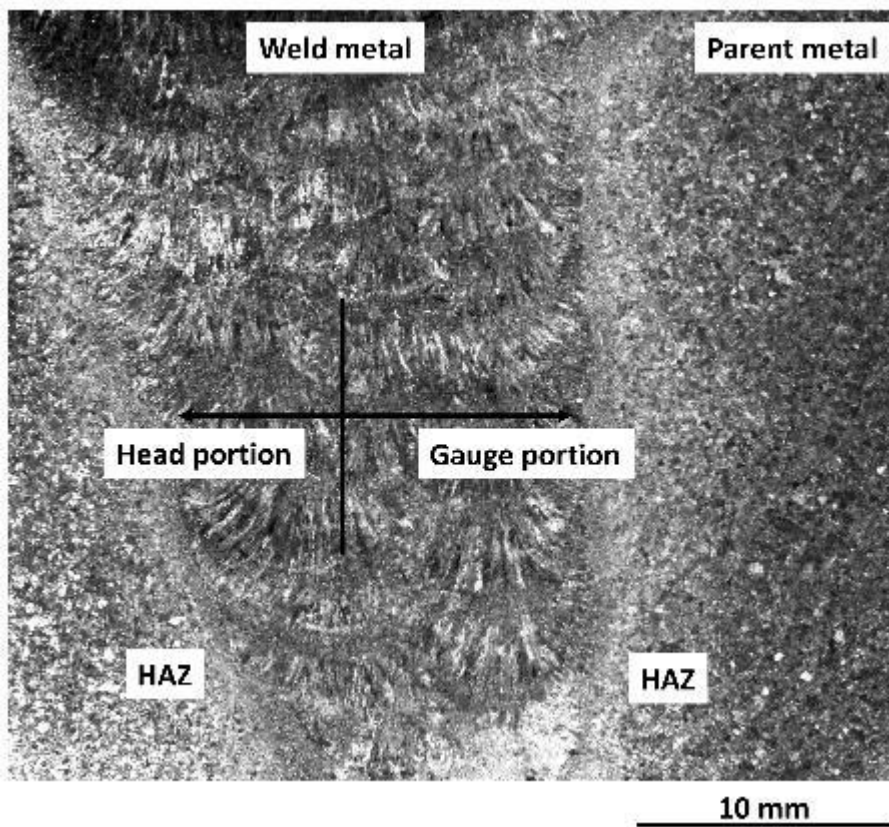
114 **Table 1. Chemical composition of the IBN-1 parent metal (wt. %, balance is Fe).**

C	Si	Mn	P	S	Cr	Mo	Ni
0.1	0.45	0.54	0.012	0.004	8.74	0.05	0.14
Al	B	Co	Cu	Nb	V	W	N
0.007	0.012	3.02	0.04	0.06	0.21	2.53	0.018

115

116 **2.2. Creep testing**

117 Creep test specimens were machined to a dog-bone shape with a cylindrical gauge portion
118 measuring 50 mm in length and 10 mm in diameter. The gauge portion consists of the
119 weld and the parent metals, together with the intermediate HAZ located at ~10 mm from
120 the boundary between the gauge and the head portions, Figure 1. The HAZ is
121 perpendicular to the principal stress direction to achieve a volume fraction of the weld
122 metal at ~20 % in the gauge portion.



123

124 **Figure 1. Optical macrograph giving an overview of the weld structure in the cross-**
125 **weld creep specimen.**

126 Isothermal short-term cross-weld creep tests were conducted at 650°C with a series of
127 stress levels ranging from 160 MPa to 280 MPa. The stress levels were selected based on

128 the existing experience of creep testing of MarBN steel [22], such that the specimens were
129 expected to be ruptured in different manners for a comparison in creep characteristics.
130 The specimens tested at a stress level close to 280 MPa were expected to fracture in a
131 ductile manner with rupture occurring in the parent metal. The specimens tested at a stress
132 level close to 160 MPa were chosen to fracture in the HAZ.

133 The testing machine was equipped with high temperature Linear Variable Displacement
134 Transformers (LVDT) to continuously monitor the elongation of specimens, and a
135 resistance-heating furnace enabling a quasi-homogeneous testing temperature of up to
136 800°C. The measured creep strain represents the integral accumulated creep strain of the
137 entire cross-weld material within the gauge length. Three thermocouples were attached
138 to the specimen inside the furnace to track the operating temperature. Note that the
139 thermal gradient between both sample extremities was less than 2°C. Prior to testing,
140 thermal loading was first performed with a rate of 40°C/min until reaching the target
141 temperature. After stabilization of the furnace temperature (~30 minutes), creep tests were
142 conducted until the macroscopic failure of samples.

143 **2.3. Metallographic examination**

144 Gauge portions of the creep ruptured specimens were sectioned from the head and along
145 the longitudinal direction for detailed metallographic examination of the cross-sections.
146 The specimens were prepared using conventional metallographic preparation methods,
147 which involved mounting in electrically conductive Bakelite, grinding on SiC with water
148 to a 1200 grit finish, polishing on standard polishing cloths using 6 µm and 1 µm diamond
149 suspensions and a final chemo-mechanical polishing process using a suspension of 0.06

150 μm colloidal silica in water. An as-fabricated weld was also prepared using the same
151 procedure to provide details of the initial microstructure before creep exposure.

152 Hardness testing was conducted on the as-fabricated weld using a loading weight of 10 kg
153 and a dwell time of 10 s using a Struers[®] Durascan[®] 70 hardness testing system equipped
154 with a Vickers indenter. Seven individual measurements were conducted to obtain the
155 average value of hardness from both the weld and the parent metals. Hardness mapping
156 was also undertaken on the as-fabricated weld and on creep ruptured specimens in the
157 regions adjacent to the rupture surface using a loading weight of 0.2 kg and a dwell time
158 of 10 s using the identical hardness testing system. Vickers hardness indents were
159 distributed on a square grid with a spacing of 0.1 mm.

160 Fractography examination was performed on the fracture surfaces of creep ruptured
161 specimens using a JEOL[®] JSM-7800F Field Emission Gun (FEG) Scanning Electron
162 Microscope (SEM) at an accelerating voltage of 5 kV. Grain orientation mapping of the
163 matrix was undertaken by performing EBSD mapping at an accelerating voltage of 20 kV
164 using an Oxford Instruments[®] Nordlys[®] MAX² camera in the JEOL[®] JSM-7800F FEG-
165 SEM. EBSD maps were collected on the cross-section of the as-fabricated weld and
166 adjacent to the rupture surface of creep fractured specimens at a step size of 2 μm with a
167 size of 1000 \times 1000 μm to provide an overview of the microstructure. EBSD mapping
168 was also performed at a finer step size of 0.1 μm to obtain details of the microstructure.
169 The distribution of secondary precipitates in identical regions to where EBSD mapping
170 was conducted was characterised using ion induced Secondary Electron (SE) imaging in
171 a FEI[®] Nova Nanolab[®] 600 Focused Ion Beam (FIB) FEG-SEM. The ion beam was
172 operated at an accelerating voltage of 30 kV with XeF₂ gas etching used to enhance the
173 contrast differential between precipitates and matrix [19,23].

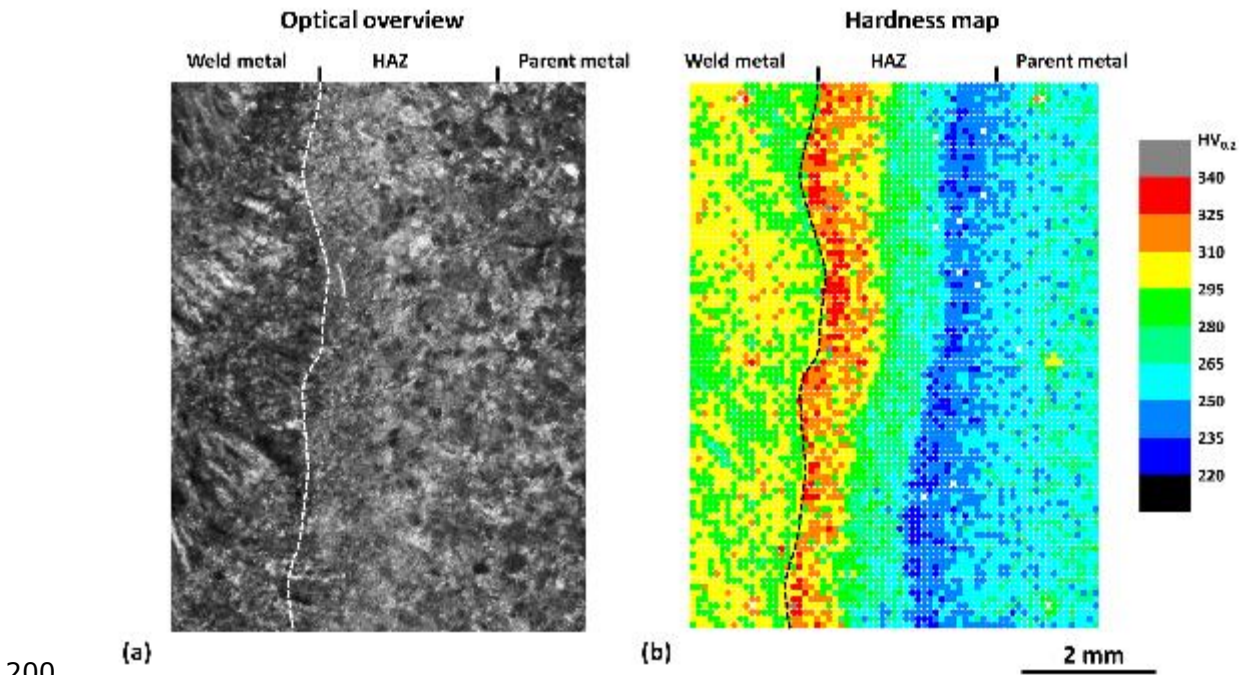
174 Thin-foil specimens were extracted from site-specific locations where the correlative
175 EBSD/ion induced SE analysis was conducted using an *in-situ* lift-out technique [24] in
176 a FEI® Nova Nanolab® 600 FIB/FEG-SEM. The thinning of specimens was performed at
177 an accelerating voltage of 30 kV with a beam current decreasing to 0.1 nA, followed by
178 a final cleaning process performed at an accelerating voltage of 5 kV. The extracted thin-
179 foil specimens were investigated using Bright Field Scanning Transmission Electron
180 Microscopy (BF-STEM) in a FEI® Tecnai® F20 Transmission Electron Microscope
181 (TEM) at an accelerating voltage of 200 kV. Secondary precipitates were further
182 characterised using Selected Area Electron Diffraction (SAED) in combination with
183 Energy Dispersive X-ray (EDX) spectroscopy using an Oxford Instruments® X-Max 80^N
184 TLE EDX system.

185 **3. RESULTS**

186 **3.1. Microstructural distribution in the as-fabricated condition**

187 The hardness of the weld and the parent metals were measured using macro-hardness
188 testing. The hardness of the weld and the parent metals were determined to be 290 ± 4 and
189 249 ± 2 HV₁₀, respectively. The value of hardness obtained from the parent metal is
190 consistent with the previous reports from similar MarBN steels [25,26]. The weld metal
191 exhibited a higher level of hardness as compared to the parent metal. This is possibly
192 attributed to a more refined martensitic microstructure as formed in the weld metal after
193 rapid solidification and cooling during the welding stage, and a less homogenised and
194 recovered martensitic substructure due to a lack of normalisation treatment as compared
195 to the parent metal.

196 The microstructural variation in the as-fabricated weld without creep exposure was
197 further characterised using hardness mapping analysis at a different loading weight of 0.2
198 kg. Figure 2 demonstrates a macro optical micrograph providing an overview of the weld
199 microstructure and a hardness map from the same region.

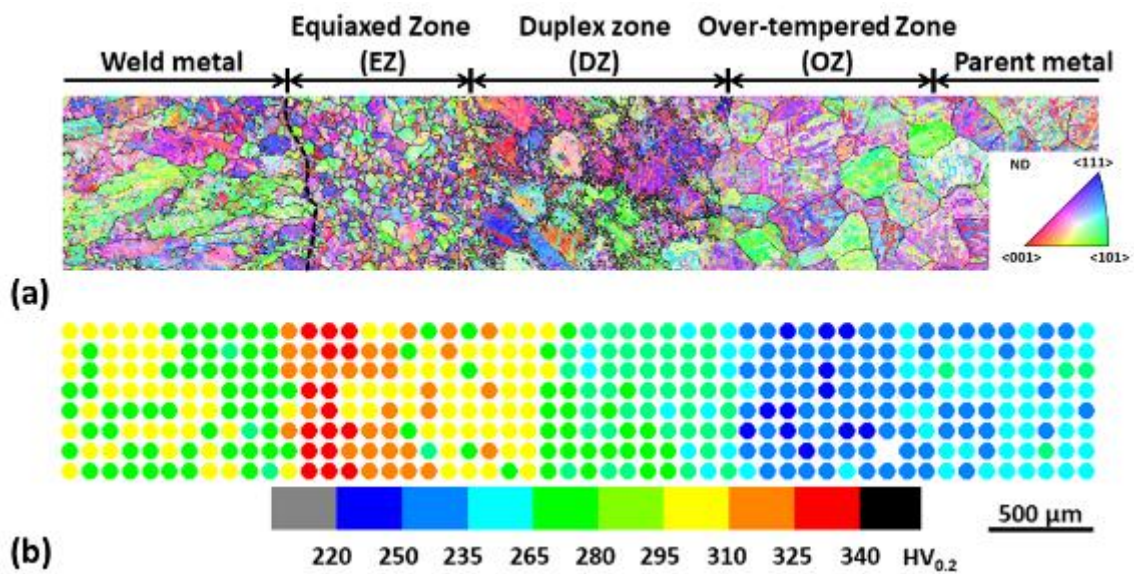


200 (a) (b) 2 mm

201 **Figure 2. (a) A macro optical micrograph demonstrating the variation of**
202 **microstructure between the weld metal, the HAZ and the parent metal. (b) A**
203 **hardness map showing the variation in hardness from the same region.**

204 From the hardness map, the weld metal has a higher level of hardness at 296 ± 9 HV_{0.2} as
205 compared to the parent metal measured with a hardness of 261 ± 9 HV_{0.2}. These values of
206 hardness are lower than the values obtained at a loading weight of 10 kg. This is
207 attributable to the different measuring volumes that were achieved at a different loading
208 weight. No significant variation in hardness was observed in the HAZ along the direction

209 parallel to the fusion boundary (i.e. from bottom to top in Figure 2), whilst a decrease in
 210 hardness was clearly observed as the distance from the fusion boundary increased.
 211 The distribution in hardness in the HAZ region suggests significant microstructural
 212 variation as a function of distance from the fusion boundary. Correlative EBSD analysis
 213 was further conducted to detail the microstructural gradient in the HAZ, Figure 3.



214
 215 **Figure 3. (a) An EBSD map providing an overview of the tempered martensitic**
 216 **matrix in as-fabricated IBN-1 weld. The grain boundaries with a misorientation**
 217 **range between 20° and 50° are outlined by solid lines. (b) A correlative hardness**
 218 **map showing the variation of hardness in the identical region is also included for**
 219 **comparison.**

220 Due to a Kurdjumov-Sachs orientation relationship preserved between the martensitic (α')
 221 and the parental austenitic (γ) phases during martensitic transformation, the austenitic
 222 grain structure was characterised from EBSD maps using a boundary misorientation
 223 range between 20° and 50° [20,27,28]. Figure 3a shows that columnar and equiaxed

224 austenitic structures are presented in the weld and the parent metals, respectively. The
225 columnar grains in the weld metal are typically 50-200 μm in width and over 1000 μm in
226 length, whilst the equiaxed grains in the parent metal are predominantly 100-500 μm in
227 diameter. In the HAZ region close to the fusion boundary, the grain structure was found
228 to have transformed from a refined, equiaxed morphology in the region <1 mm from the
229 fusion boundary to a duplex grain structure containing small austenite grain ‘necklaces’
230 around pre-existing PAGBs in the region 1-2 mm from the fusion boundary. The equiaxed
231 grains in the region <1 mm from the fusion boundary are predominantly <150 μm in
232 diameter, whereas the austenite “necklace” grains on the initial PAGBs are <20 μm in
233 diameter in the regions 1-2 mm from the fusion boundary. The microstructural gradient
234 in the HAZ was further correlated with the variation in hardness as demonstrated in Figure
235 3b. The hardness map demonstrates that the region with a refined, equiaxed grain
236 structure has a higher level of hardness measuring $305\pm 16 \text{ HV}_{0.2}$, whereas the region
237 showing a duplex grain structure has a lower level of hardness of $262\pm 17 \text{ HV}_{0.2}$. The grain
238 structure in the regions ~2-3 mm from the fusion boundary is not significantly varied from
239 the parent metal, whereas the hardness was lower, with an average value measuring 247 ± 9
240 $\text{HV}_{0.2}$.

241 The microstructure in the HAZ of as-fabricated IBN-1 weld is further correlated with the
242 microstructure produced by the simulation of weld thermal cycles as previously reported
243 in [21], Table 2.

244 **Table 2. A comparison in microstructure between the HAZ of the as-fabricated IBN-**
245 **1 weld and the simulated HAZ material produced using dilatometry-based**
246 **simulations of weld thermal cycle [21].**

Simulated HAZ material [21]		As-fabricated weld		Classification
Peak temperature	Characteristics of microstructure	Distance from fusion boundary	Characteristics of microstructure	
>1200°C	Equiaxed morphology, grain size <100 µm;	<1 mm	Equiaxed morphology, grain size <150 µm;	Equiaxed Zone (EZ)
1000 - 1200°C	Duplex microstructure characterised by refined grains on the pre-existing PAGBs;	1 - 2 mm	Duplex microstructure characterised by small grains (<20 µm) on the pre-existing PAGBs;	Duplex Zone (DZ)
<1000°C	Equiaxed morphology, grain size >300 µm;	2 - 3 mm	Equiaxed morphology, grain size 100 - 500 µm;	Over-tempered Zone (OZ)

247

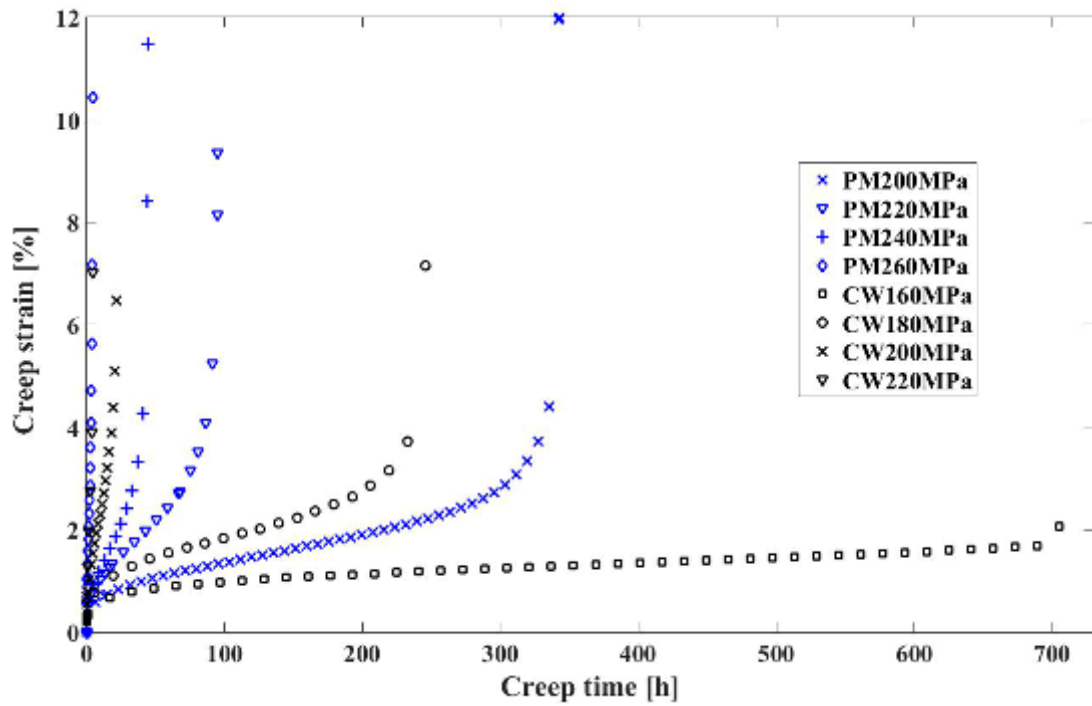
248 Table 2 demonstrates that the distribution of HAZ microstructure as a function of the
249 distance from fusion boundary is in strong agreement with the microstructure in the HAZ
250 simulated materials as a function of peak temperature. This suggests that the
251 microstructure in the weld HAZ can be classified based on the gradient of heat input as a
252 function of the distance from fusion boundary. As a result, the weld HAZ was classified
253 as three critical sub-regions, the Equiaxed Zone (EZ), the Duplex Zone (DZ) and the
254 Over-tempered Zone (OZ) (Figure 3). A detailed description of the microstructure in these
255 sub-regions is not the focus of the investigation in the current research, as this has been
256 reported elsewhere in a previous study [21]. However, it has been clearly demonstrated
257 in the current research that the microstructure of the HAZ in MarBN steel welds is
258 different from the conventional understanding of the HAZs in low alloy Cr-Mo steels,
259 which are commonly classified into Coarse-grain (CG), Fine-grain (FG), Inter-critical
260 (IC) and Over-tempered (OT) regions [11].

261 **3.2 Mechanical behaviour**

262 Creep responses for cross-weld specimens are compared with the parent metal specimens
263 as previously reported in [22], Figure 4. The corresponding creep properties are

264 summarised in Table 3. These include the Steady-State Creep Rate (SSCR), the time to
265 fracture τ_f , ductility ϵ_f , and the Reduction of Area (RA).

266 It can be seen that the three typical creep stages (a primary creep stage followed by an
267 apparently steady-state creep deformation and an accelerating tertiary creep stage) are
268 clearly visible for all tests under investigation. The creep results demonstrate that the
269 minimum creep strain rate increases with the increase of stress while creep rupture time
270 decreases as stress increased. At the medium stress level of 200 MPa and 220 MPa, SSCR
271 values for cross-weld are 26-fold higher than the parent metal, whilst the time to rupture
272 is 14- to 18-fold shorter as compared to the parent metal. This clearly indicates a lower
273 creep resistance of the cross-weld specimen as compared to the parent metal specimen.
274 This finding applies to all stress levels selected for this investigation. Moreover, no
275 significant changes have been observed when comparing both values of the area reduction
276 and ductility reported for both parent metal and cross-weld.



277

278 **Figure 4. Strain-time curves for creep tests conducted on parent metal (PM) and**
 279 **cross-weld (CW) specimens at 650°C.**

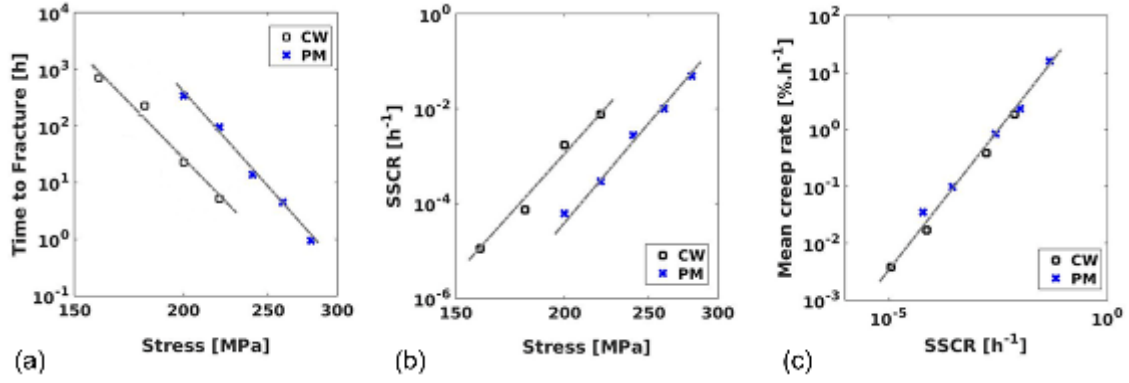
280 **Table 3. Material creep properties for parent metal (PM) and cross-weld (CW)**
 281 **specimens selected at different stress levels.**

σ [MPa]	Material	SSCR [$10^{-5} \times h^{-1}$]	τ_f [h]	ϵ_f [%]	RA [%]
160	PM	-	-	-	-
	CW	1.13	705.56	2.66	14.44
180	PM	-	-	-	-
	CW	7.31	248.35	5.62	42.24
200	PM	6.12	342.91	11.93	62.05
	CW	170.02	22.96	7.86	73.79
220	PM	29.12	95.47	9.36	73.68
	CW	770.15	5.14	11.35	80.29
240	PM	280.32	13.73	11.48	74.29
	CW	-	-	-	-
260	PM	1000.21	4.43	10.48	75.11
	CW	-	-	-	-
280	PM	4851.23	0.94	14.88	81.08
	CW	-	-	-	-

282

283 All aforementioned creep rupture characteristics of the parent metal and cross-weld are
284 gathered for comparison in Figure 5 and summarised in Table 4 in the form of power-law
285 (relating the time-to-rupture or SSCR to the stress) and Monkman-Grant (relating the
286 mean creep rate to SSCR) relationships. Figures 5a and 5b show that the cross-weld
287 specimens have a considerably shorter creep life and a higher creep strain rate as
288 compared to the parent metal specimens, whilst Figure 5c reveals a similar Monkman-
289 Grant (MG) relationship for both the cross-weld and the parent metal specimens. In
290 addition, no significant differences were observed for the apparent stress and MG
291 exponents between the cross-weld and the parent metal specimens, as detailed in Table
292 4. The parent metal specimens show a slightly higher stress exponent value, m , as
293 compared to the cross-weld specimen, whilst the stress exponent value, n , is slightly
294 higher for the cross-weld specimen. The MG exponent, ξ , for the cross-weld specimens
295 turns out to be 0.95, whilst that of the parent metal specimens is ~ 0.87 .

296 Additional calculations were conducted on separate groups of the specimens tested at
297 different stress levels, which appear to exhibit different creep behaviour as indicated by
298 an evident deviation from the linear relationship as shown in Figure 5a. The stress
299 exponent value, m , was obtained at 8.87 and 15.70 for the specimens tested at 160/180
300 MPa and 200/220 MPa, respectively. A close value of stress exponent, m , between the
301 cross-weld specimens tested at a higher level of stress and the parent metal specimens
302 suggests similar creep behaviour for the specimens tested at the identical conditions,
303 whilst the creep behaviour of the specimens tested at 160/180 MPa may be different as
304 proposed by a considerable discrepancy in stress exponent value with the parent metal
305 specimens. As a result, creep life is significantly shortened to a higher extent for the cross-
306 weld specimens tested at a lower stress level (e.g. 160 and 180 MPa).



307

308

309

310

311

312

Figure 5. (a) Time to fracture vs. applied stress. (b) SSCR vs. applied stress. (c) Mean creep rate (ϵ_f/τ_f) vs. SSCR of IBN-1 cross-weld (CW) and parent metal (PM) specimens.

Table 4. Apparent values of creep function coefficients for parent metal (PM) and cross-weld (CW) specimens.

Material	Time to fracture		Steady-state creep rate		Monkman-Grant relationship	
	$\tau_f = p \sigma^{-m}$		SSCR = $q \sigma^n$		SSCR ^{ξ} = $\omega \epsilon_f/\tau_f$	
	p [(MPa) ⁻¹ ·h]	m [-]	q [(MPa·h) ⁻¹]	n [-]	ω [-]	ξ [-]
PM	7.59×10^{42}	17.53	1.07×10^{-50}	19.88	0.63	0.87
CW	2.63×10^{38}	16.08	6.47×10^{-53}	21.42	0.56	0.95

313

314

3.3. Creep rupture behaviour of cross-weld specimen at different stress levels

315

316

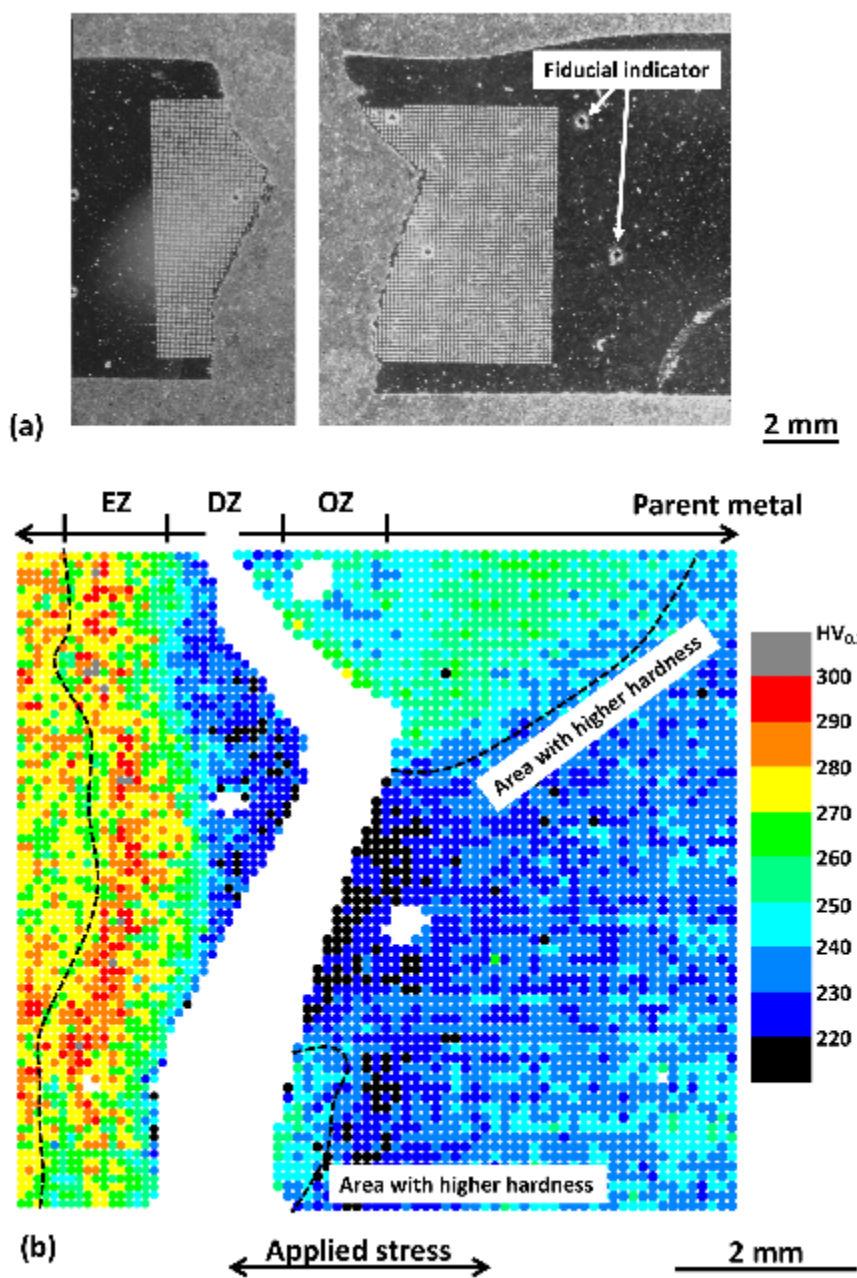
317

The microstructures in the creep exposed cross-weld specimens were investigated using hardness mapping analysis in combination with fractography examination to understand the correlation between the weld microstructure and the creep rupture behaviour.

318

319

Hardness mapping was conducted in the region close to the rupture surface to reveal the variation in hardness after creep testing at 650°C and 160 MPa, Figure 6.



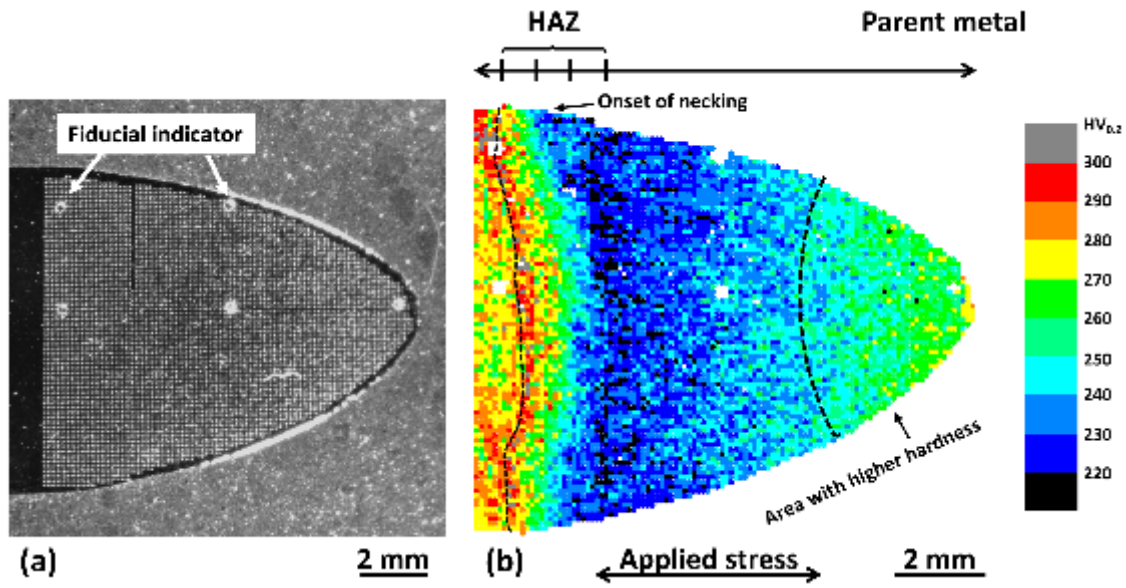
320

321 **Figure 6. (a) Photographs showing the cross-section of a creep ruptured cross-weld**
 322 **specimen after creep testing at 650°C and 160 MPa for 705 hours prior to hardness**
 323 **mapping analysis. (b) A hardness map showing the variation of hardness in the**
 324 **region of analysis.**

325 Figure 6b shows that the hardness of the weld metal ranges between 238 and 299 HV_{0.2}
 326 with an average hardness measuring 274±9 HV_{0.2}, whereas the hardness of the parent

327 metal is in the range of 221-258 HV_{0.2} with an average value obtained at 236±6 HV_{0.2}.
328 The hardness in the HAZ decreases from 312 HV_{0.2} to 205 HV_{0.2} with distance from the
329 fusion boundary. The rupture surface is located at ~1.0-2.5 mm from the fusion boundary
330 with a zig-zag crack path. The rupture surface is aligned at ~90° to the principal stress
331 direction close to the outer surface (bottom), whereas it is ~70° and ~45° to the principal
332 stress direction in the centre and close to the other side (top), respectively. The hardness
333 in the regions extending from the portions at ~90° and ~45° is in the range of 232-253
334 HV_{0.2} and 235-273 HV_{0.2}, respectively. The hardness measured from the regions
335 extending from the portion at ~70° to the principal stress direction is lower and in the
336 range between 206 and 237 HV_{0.2}. The angle of the rupture surface is related to the
337 microstructure of the weld and the local stress state during creep testing. However, it is
338 also affected by the other factors such as the surface condition of the specimen and the
339 experimental condition of creep test. Detailed examination of the creep ruptured cross-
340 weld specimen is required to reveal the underlying reasons for the rupture of specimens.

341 Hardness mapping analysis was further conducted on the creep ruptured specimen which
342 was tested at 650°C and 200 MPa, Figure 7.



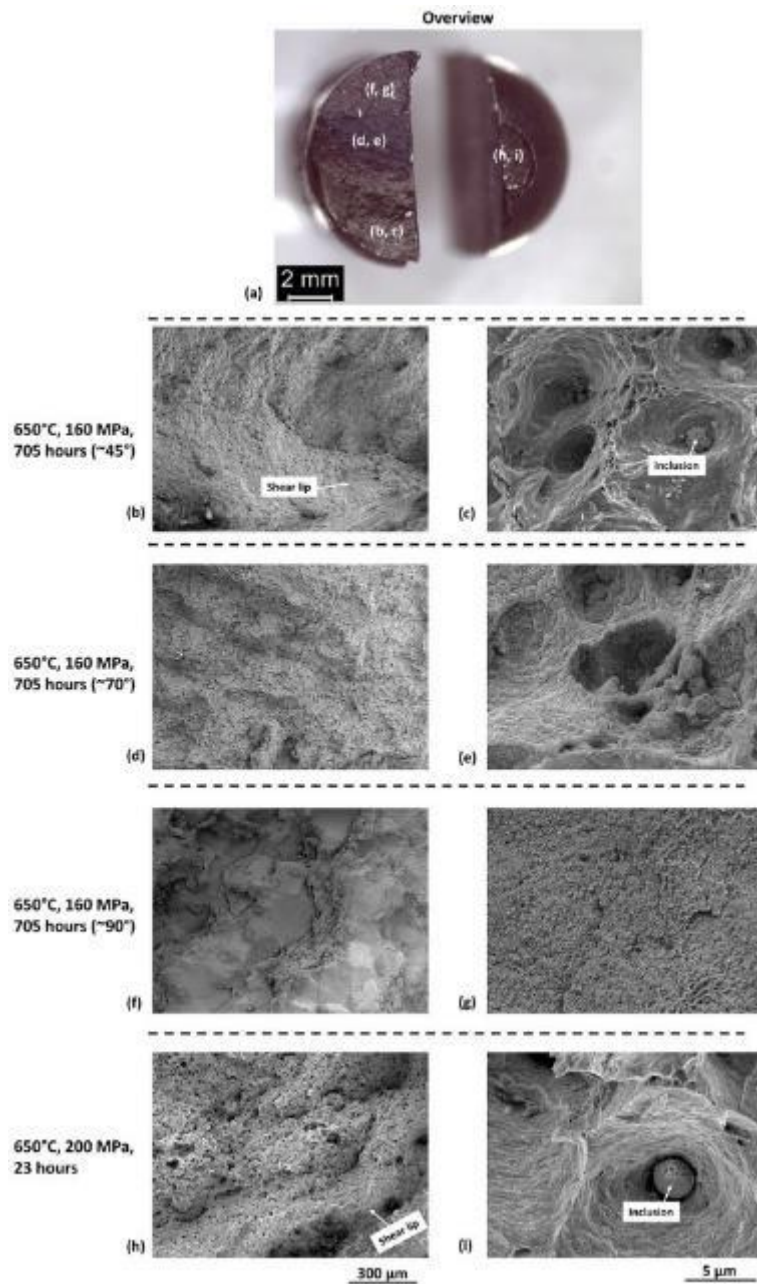
343

344 **Figure 7. (a) A photograph showing the cross-section of a creep ruptured cross-weld**
 345 **specimen after creep testing at 650°C and 200 MPa for 23 hours prior to hardness**
 346 **mapping analysis.**

347 The hardness measured from the weld and parent metals (Figure 7) is similar to the
 348 specimen ruptured at 160 MPa. The hardness of the weld metal is in the range between
 349 253 and 314 HV_{0.2} with an average value measuring 279±9 HV_{0.2}, whereas the hardness
 350 of the parent metal is between 219 and 269 HV_{0.2} with an average value obtained at 241±8
 351 HV_{0.2}. The hardness in the HAZ is similar to the specimen tested at 650°C and 160 MPa
 352 and is decreased from 320 to 205 HV_{0.2} as the distance from the fusion boundary
 353 increases. The rupture surface is located at ~11 mm from the fusion boundary, with
 354 substantial necking which also includes an increase in hardness to a maximum value of
 355 285 HV_{0.2}.

356 Fractographic examination was conducted on the rupture surfaces to understand the
 357 fracture behaviour of the creep exposed specimens. Figure 8 demonstrates the topography
 358 of the rupture surface in the specimens tested at 650°C/160 MPa and 650°C/200 MPa.

359 Figures 8b-8g demonstrate that the rupture surface in the specimen tested at 650°C and
360 160 MPa has changed from an intergranular to a ductile dimpled topography from the
361 regions with an angle of at ~90° to ~70° and ~45° to the principal stress direction. The
362 intergranular surface at ~90° is not similar to the characteristics of typical faceted surfaces
363 formed by intergranular fracture [29], but it is covered by scale-like features that are
364 possibly formed by oxidation (Figure 8g). The dimples in the region ~70°/~45° to the
365 principal stress direction are typically 3-10 μm in diameter and occasionally associated
366 with inclusion particles (e.g. Figure 8c), which is consistent with the existing report of
367 plastic damage associated with secondary phase particles [30]. The rupture surface of the
368 specimen tested at 650°C and 200 MPa is composed of a dimpled central region in
369 combination with a shear lip close to the outer surface (Figure 8h). Figure 8i demonstrates
370 that the dimples in the central region are similar in size as compared to the specimen
371 tested at 650°C and 160 MPa and occasionally associated with inclusions.



372

373 **Figure 8. (a) An optical overview of rupture surface in the specimens tested at (left)**
 374 **650°C/160 MPa and (right) 650°C/200 MPa. Topography of the rupture surface is**
 375 **further detailed for the regions with an angle of (b, c) ~45°, (d, e) ~70° and (f, g) ~90°**
 376 **to the principal stress direction in the specimen tested at 650°C/160 MPa and (h, i)**
 377 **the rupture surface after creep testing at 650°C/200 MPa.**

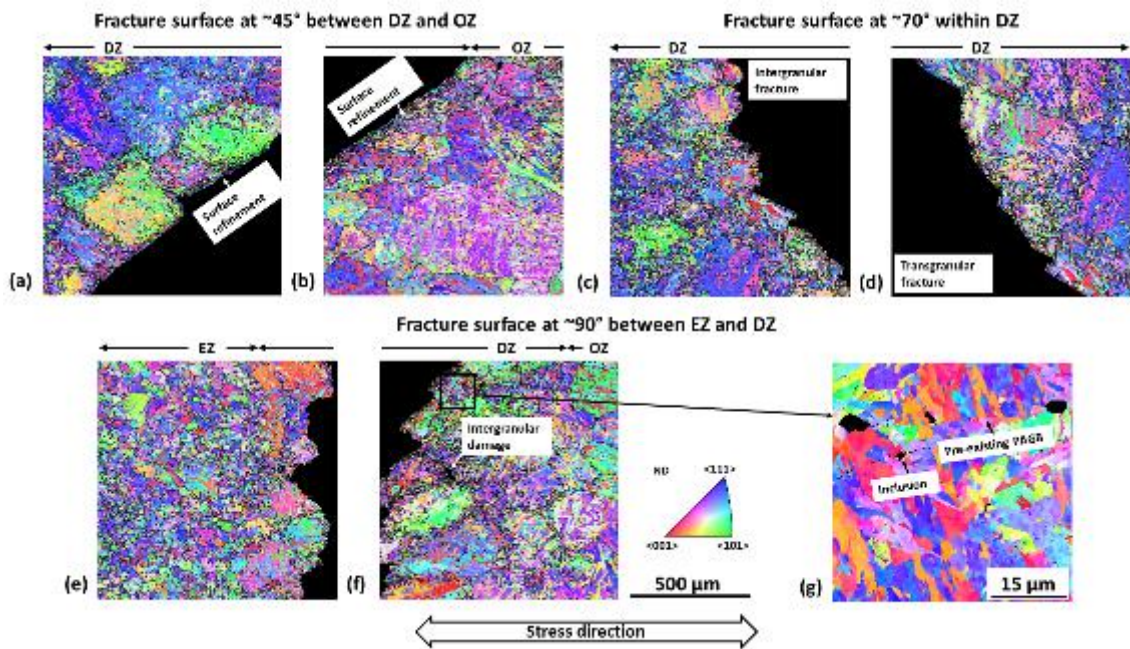
378 Previous studies that were systematically conducted at various creep test conditions have
379 revealed a variation in rupture behaviour from catastrophic HAZ failure occurring in the
380 ‘Type IV’ zone, to ductile rupture of the parent metal against a decreasing testing
381 temperature and/or an increasing stress level for the welds with a parent metal of similar
382 materials [11,31]. This trend in creep rupture behaviour against the variation of creep test
383 condition is consistent with the creep behaviour of IBN-1 steel welds between the tests
384 conducted at 650°C and 160/200 MPa here. The IBN-1 weld tested at 200 MPa
385 demonstrates similar creep behaviour to the IBN-1 parent materials from the identical
386 industrial heat in tests at similar conditions, where dislocation climb acts as the dominant
387 rate controlling factor for creep deformation [22]. However, the specimen tested at 650°C
388 and 160 MPa demonstrates distinctively different creep rupture behaviour as indicated by
389 an intergranular rupture surface located in the HAZ. Detailed metallographic examination
390 is required to obtain an in-depth understanding of metallurgical causes for the occurrence
391 of intergranular HAZ failure.

392 **3.4. The influence of HAZ microstructure on creep rupture**

393 EBSD mapping was conducted in local areas close to the rupture surface in the HAZ of
394 the specimen tested at 650°C and 160 MPa, Figure 9.

395 Figure 9 clearly demonstrates the correlation between HAZ microstructure and the
396 location of rupture surface. The surface portion at $\sim 45^\circ$ to the principal stress direction is
397 close to the boundary between the DZ and the OZ, whereas the portion at $\sim 70^\circ$ is located
398 within the DZ. The surface portion at $\sim 45^\circ$ is transgranular and relatively straight (Figures
399 9a and 9b), whereas the surface portion at $\sim 70^\circ$ is transformed from intergranular (Figure
400 9c) to transgranular (Figure 9d) when moving from the region adjacent to the surface

401 portions at $\sim 90^\circ$ to the region close to the portion at $\sim 45^\circ$. However, the surface portion
 402 at $\sim 90^\circ$ is clearly intergranular and formed along the ‘necklace’ of pre-existing PAGBs
 403 as marked by the traces of refined grains $<20\ \mu\text{m}$ in diameter (Figures 9e and 9f). The
 404 location of the intergranular surface portion has been confirmed in the region close to the
 405 boundary between the EZ and the DZ, with a distance of $\sim 1.1\ \text{mm}$ from the fusion
 406 boundary. The presence of secondary damage was also observed in the intergranular
 407 region on pre-existing PAGBs and triple points (Figures 9f and 9g) in the area close to
 408 the rupture surface.



409

410 **Figure 9. EBSD maps showing the microstructure in the regions close to rupture**
 411 **surface at (a, b) $\sim 45^\circ$, (c, d) $\sim 70^\circ$ and (e, f) $\sim 90^\circ$ to the principal stress direction in**
 412 **the specimen tested at 650°C and $160\ \text{MPa}$. (g) An EBSD map collected at a higher**
 413 **resolution detailing the correlation between microstructure and secondary damage**
 414 **close to rupture surface. The grain boundaries with a misorientation range between**
 415 **20° and 50° are outlined by solid lines.**

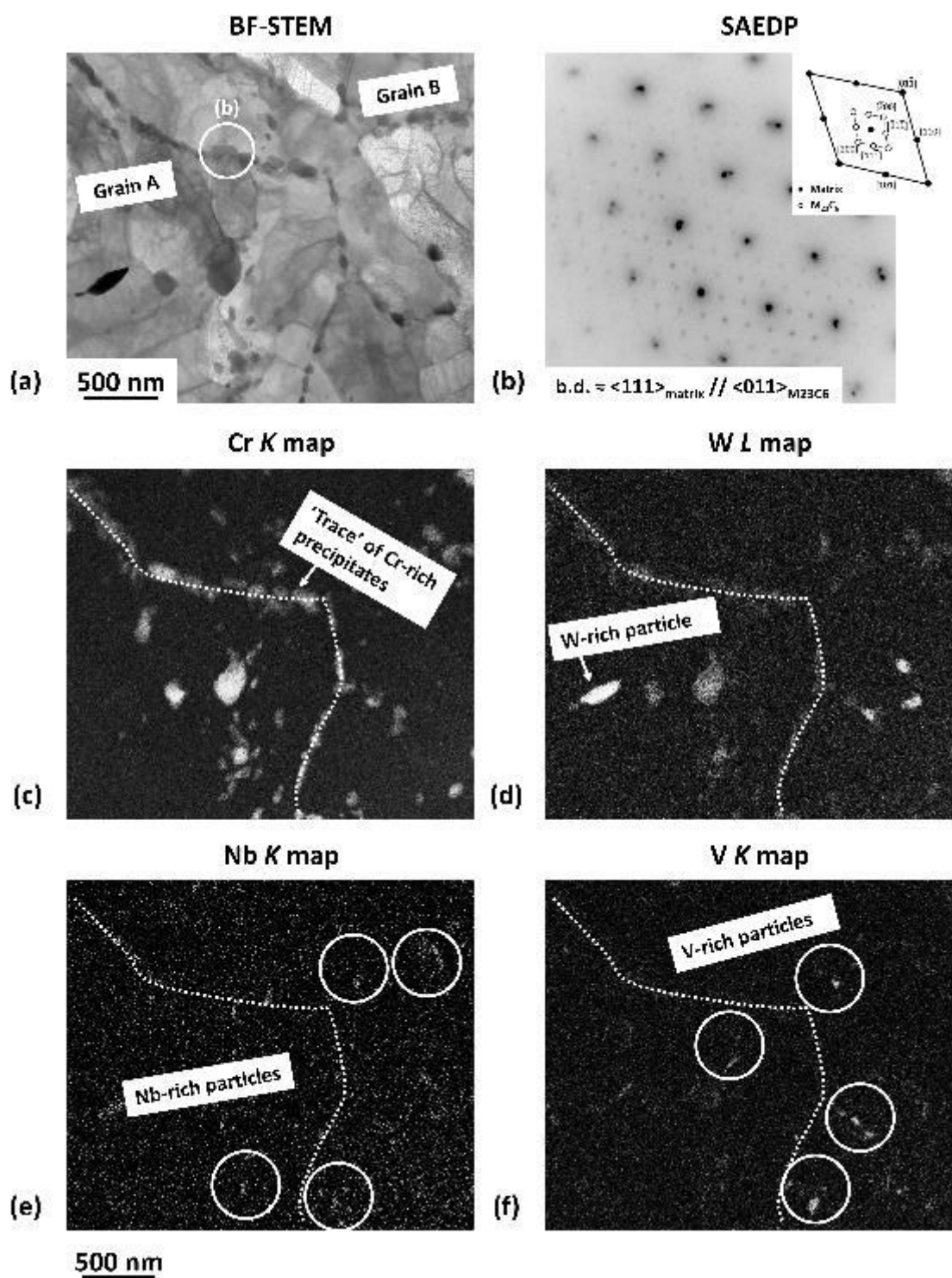
416 The initial microstructure in the HAZ of the as-fabricated IBN-1 weld was further
417 investigated in detail to identify the cause of intergranular creep rupture from a
418 metallurgical perspective. Figure 10 demonstrates the correlative micrographs obtained
419 from the DZ regions in the as-fabricated weld at a similar distance from the fusion
420 boundary as the location of the rupture surface using EBSD and ion induced SE imaging.

421 Figure 10a demonstrates an evident transition between the EZ and DZ at ~1 mm from the
422 fusion boundary as indicated by the change in microstructure. One region (Region 1)
423 selected for correlative EBSD/ion induced SE analysis is close to the boundary between
424 the EZ and the DZ with a similar distance from the fusion boundary as the rupture surface
425 (Figure 9) to compare with the microstructure in another region (Region 2) further away
426 from the fusion boundary (~1.3 mm). EBSD mapping analysis (Figures 10b and 10d)
427 reveals the elongated blocks that are a few microns in width within the martensitic
428 substructure of the fine and coarse grains within the DZ, whereas the correlative ion
429 induced SE micrographs (Figures 10c and 10e) demonstrate the precipitate particles that
430 are preferentially distributed on substructure boundaries. Notably, the boundary of the
431 refined grains formed along a pre-existing PAGB (e.g. Grain B) are consistently
432 decorated by precipitate particles with a diameter of <150 nm in Region 1 (Figure 10c),
433 whereas the boundary of the refined grains in Region 2 (e.g. Grain D) are decorated to a
434 lesser extent (Figure 10d). This is attributed to an incomplete dissolution of the pre-
435 existing precipitate particles in the regions further away from the fusion boundary due to
436 a lower experienced peak temperature, which consumes the carbide forming elements in
437 the matrix and mitigates a further formation of grain boundary precipitates as previously
438 reported in Grade 92 steel weld [20].

446 **micrographs were inverted in grey scale for a clear visualisation of the precipitates**
447 **as bright particles.**

448 The precipitates on the boundary of a refined grain (Grain B) in Region 1 were further
449 extracted using the FIB lift-out technique for high-resolution analysis in TEM using
450 SAED and STEM-EDX. Figure 11 displays a BF-STEM micrograph collected from the
451 boundary of Grain B with the SAEDPs and EDX maps collected from precipitates and
452 the surrounding matrix.

453 The martensitic substructure is predominantly composed of laths that are $<1\ \mu\text{m}$ in width
454 in combination with a high density of dislocations within the lath interiors. The majority
455 of the precipitate particles distributed on the boundaries of Grain B are $<150\ \text{nm}$ in
456 diameter and have an FCC lattice structure similar to the M_{23}C_6 carbides [32]. A crystal
457 orientation relationship of $\{011\}_{\text{precipitate}} // \{111\}_{\text{matrix}}$, $\langle 111 \rangle_{\text{precipitate}} // \langle 011 \rangle_{\text{matrix}}$ was
458 also confirmed between the precipitates and the matrix (Figure 11b). Figures 11c-11f
459 further demonstrate that the precipitates distributed on the boundary of Grain B have a
460 similar chemistry to the M_{23}C_6 carbides that are abundant in Cr in combination with a
461 minor level of W [33]. The presence of precipitate particles that are abundant in W or
462 Nb/V was also observed at a minor level (Figures 11d-11f). The chemical compositions
463 of the W-rich and Nb/V-rich precipitates are similar to the chemistry of Laves and MX
464 carbonitrides [34,35], respectively.



465

466 Figure 11. (a) A BF-STEM micrograph of the detailed martensitic microstructure
 467 in the region adjacent to the boundary of Grain B (Figure 10) and (b) an SAEDP
 468 collected from a precipitate particle with grey scale inverted for the visualisation of

469 **pattern. (c-f) Correlative EDX maps demonstrating the distribution of elements in**
470 **the precipitates and the surrounding matrix.**

471 **4. DISCUSSION**

472 The dimpled rupture surface on the specimen tested at 650°C and 200 MPa is formed by
473 ductile fracture due to significant stress concentration in the necked region, similar to that
474 as previously observed in parent metal specimens [22]. However, the rupture behaviour
475 of the IBN-1 weld tested at 650°C and 160 MPa is distinctively different and is marked
476 by an intergranular rupture surface located within the HAZ. Based on detailed
477 metallographic examinations of the specimens before and after creep exposure, the
478 rupture surface generated at an applied stress of 160 MPa was found to be located in the
479 region close to the boundary between EZ and DZ.

480 The EZ and DZ are distinctively classified by an evident transition in prior austenite grain
481 morphology from an equiaxed microstructure to a duplex structure containing refined
482 PAGs distributed on the initial PAGBs (Figure 10). These fine grains are likely to form
483 via a diffusive transformation mechanism that is initiated from the PAGBs due to a lower
484 energy for formation. This is evidenced by a preferential distribution of Cr-containing
485 $M_{23}C_6$ carbides on the boundary of these refined grains (Figure 10). This is caused by the
486 segregation of carbide forming elements (e.g. Cr) on the boundaries as result of diffusion
487 [38]. Similar observations were also obtained from a Fe-13%Cr-4%Ni-Mo martensitic
488 steel after diffusive austenitisation in the lower temperature regime (i.e. tempering at
489 <680°C) as previously reported [39].

490 However, it is considered that the materials in the remaining area (i.e. close to the centre
491 of PAGs) are associated with a displacive austenitisation process induced by the rapid

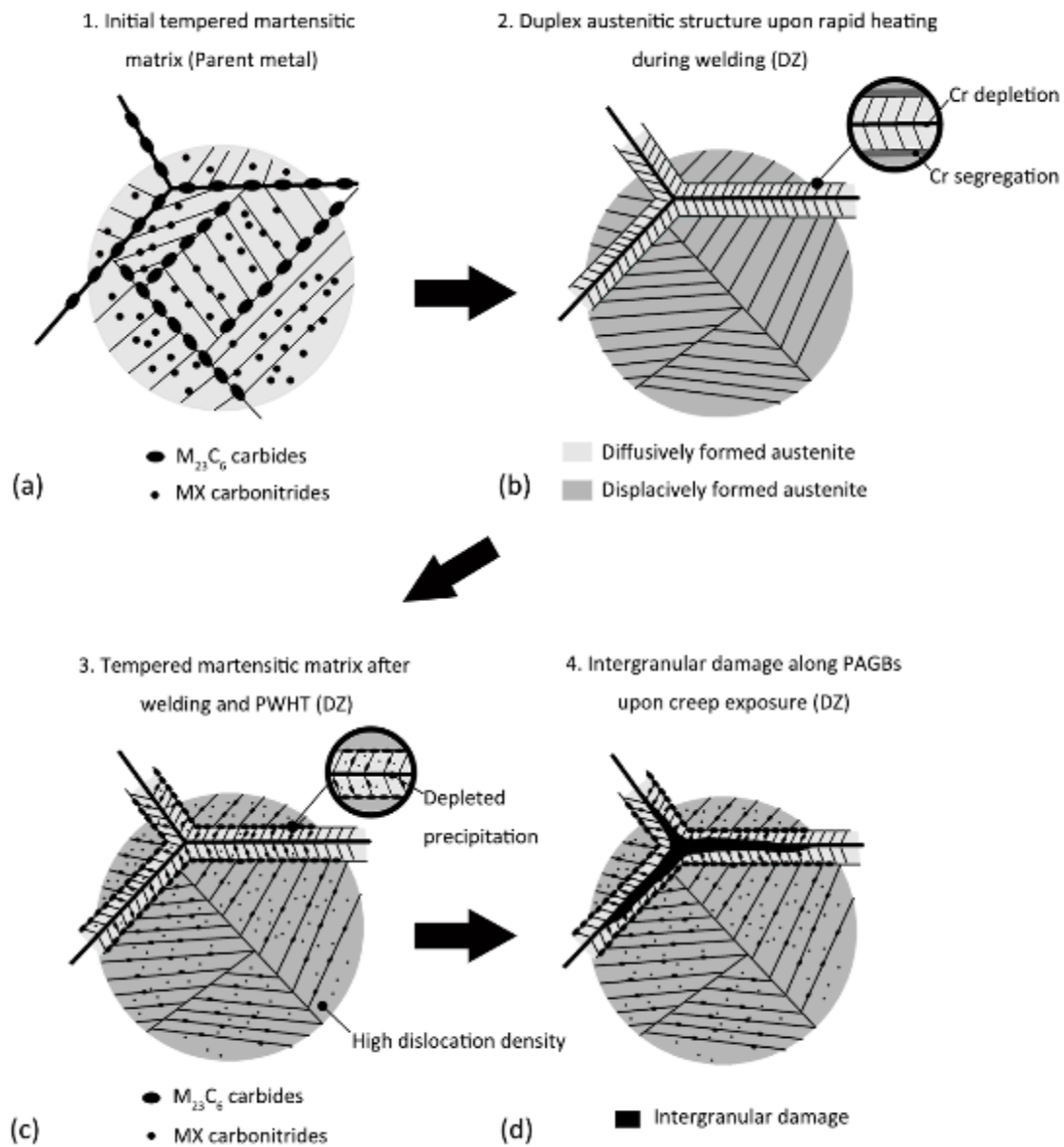
492 heating rates experienced during welding. The existing observations of displacive
493 austenitisation is comparatively limited for 9-12% Cr steels due to a relatively lower
494 heating rate associated with typical manufacturing and heat treatment processes utilised
495 for industrial applications [40]. However, fusion welding may facilitate the
496 reaustenitisation of original parent metal in the weld HAZ via a diffusionless, displacive
497 mechanism due to a high heating rate associated with weld thermal cycles that is typically
498 $>100^{\circ}\text{C/s}$ as revealed in previous research [16,18]. The critical threshold of heating rate
499 for the occurrence of displacive austenitisation has been determined to be $\sim 400^{\circ}\text{C/s}$ in a
500 0.15%C-5%Mn low alloy steel, whilst displacive austenitisation has been reported upon
501 a heating rate of 5°C/s in a Fe-13%Cr-4%Ni-Mo steel [28,41].

502 The resultant microstructure formed by displacive austenitisation has been demonstrated
503 in a previous study as a duplicated austenitic structure defined by high-angle PAGBs in
504 combination with austenitic laths sharing similar crystal orientation formed within the
505 PAG interiors. The austenitic laths with a similar crystal orientation are formed within an
506 individual PAG due to a crystallography memory effect that ‘reverses’ the orientation of
507 α/α' -Fe matrix based on a Kurdjumov-Sachs orientation relationship [42]. In the current
508 research, the microstructure observed from the central area within the PAG interiors in
509 the DZ (Figures 3 and 9) is in strong agreement with the austenitic microstructure formed
510 in a displacive manner as reported in [42]. This also explains the lack of high-angle
511 boundaries within the interiors of pre-existing PAGs in the DZ as highlighted by a range
512 of misorientation of 20° - 50° . Therefore, the duplex austenitic structure in the DZ is
513 formed via a diffusive reaustenitisation process that gives rise to refined grains along the
514 pre-existing PAGBs in combination with a displacive mechanism that reaustenitises the
515 martensitic matrix within the PAG interior. This is consistent with the experimental

516 observation as previously reported in another MarBN steel [26]. Upon further heating
517 after austenitisation is completed, the displacively formed austenite is prone to
518 recrystallisation due to a high density of dislocations in the microstructure as reported in
519 [41,42]. This further explains the presence of an equiaxed austenitic structure in the
520 regions closer to the fusion boundary as highlighted in the EZ area (Figures 3 and 9).

521 The martensite transformed from displacively formed austenite is commonly related with
522 a higher dislocation density inherited from the initial austenitic microstructure as
523 compared to the martensitic phases transformed from diffusively formed austenite
524 [41,42]. This suggests a higher dislocation density in the martensitic matrix within the
525 PAG interiors as compared to the intergranular regions showing a refined austenitic
526 structure formed by diffusive phase transformation. Therefore, the intergranular regions
527 along the PAGBs are more susceptible to damage formation by acting as the vulnerable
528 sites in the microstructure. In addition, the correlative EBSD and ion induced SE analysis
529 has revealed preferential formation of the $M_{23}C_6$ carbides on the boundaries of diffusively
530 formed austenite grains in the region close to the boundary between the EZ and DZ. This
531 is consistent with the observation from a previous study on a Fe-1%Cr-0.6%C alloy that
532 reveals the segregation of Cr accompanied with the migration of austenite grain
533 boundaries during diffusive austenitisation [38]. The diffusion of carbide forming
534 elements away from the pre-existing PAGBs further explains the scarcity of intergranular
535 $M_{23}C_6$ carbides in the areas between refined austenite grains. The depletion of precipitates
536 on PAGBs may further contribute to a higher susceptibility of intergranular damage due
537 to a lack of stabilisation effect provided by the grain boundary precipitates [33]. Figure
538 12 demonstrates a schematic diagram illustrating the critical metallurgical factors

539 associated with the formation of intergranular damage in a duplex martensitic
 540 microstructure formed by a combination of diffusive and displacive mechanisms.



541

542 **Figure 12. A schematic diagram illustrating the formation of intergranular damage**
 543 **in the microstructure of DZ after re-austenitisation from the initial microstructure**
 544 **of the parent metal prior to PWHT.**

545 **5. CONCLUSIONS**

546 The microstructural distribution in the HAZ of IBN-1 welds has been clearly determined
547 and classified into three distinctive sub-regions as the Equiaxed Zone (EZ), the Duplex
548 Zone (DZ) and the Over-tempered Zone (OZ) in the initial microstructure prior to creep
549 exposure. The microstructural and mechanical characterisations conducted after short-
550 term creep testing have further revealed an evident variation in creep behaviour between
551 the welds tested at different stress levels and the bulk materials tested at identical
552 conditions. From a mechanical point of view, a low creep resistance of the welds, as
553 compared to the parent metal, has been observed. The SSCR values for the welds were
554 found 26-fold higher than the parent metal, while the time to rupture was 14- to 18-fold
555 shorter as compared to the parent metal.

556 Detailed fractography and metallography examinations revealed a ductile rupture
557 occurred in the parent metal for the welds tested at a higher level of stress, whilst the
558 welds tested at a lower stress demonstrated a failure location in the DZ microstructure
559 close to the boundary with EZ. The initiation of such failure in IBN-1 welds was
560 dominated by intergranular cracking along the pre-existing initial PAGBs from the
561 original microstructure of the parent metal. The areas along these PAGBs acted as
562 vulnerable sites in a tempered martensitic matrix transformed from an austenitic
563 microstructure formed by a combination of diffusive and displacive mechanisms. In
564 particular, the intergranular regions were associated with higher damage susceptibility
565 due to a relatively lower strength as compared to the matrix within the PAG interiors and
566 a lack of precipitates on the PAGBs.

567 **6. ACKNOWLEDGMENTS**

568 This work was supported by the Engineering and Physical Sciences Research Council
569 (<https://www.epsrc.ac.uk/>) through the IMPULSE project (grant number:
570 EP/N509991/1). The authors gratefully acknowledge the following partners for their
571 valuable contributions: Doosan Babcock, GE Power, Uniper Technologies,
572 Metrode Products, Goodwin Steel Castings and Wyman-Gordon.
573 Specific acknowledgments to Dr Paul Robb (Doosan Babcock) for providing the test
574 material and welding procedure. The authors also acknowledge use of facilities within
575 the Loughborough Materials Characterisation Centre.

576 **7. DATA AVAILABILITY**

577 The raw/processed data required to reproduce these findings cannot be shared at this time
578 as the data also forms part of an ongoing study.

579 **8. REFERENCES**

- 580 [1] M. Taneike, F. Abe, K. Sawada, Creep-strengthening of steel at high
581 temperatures using nano-sized carbonitride dispersions, *Nature*. 424 (2003) 294–296.
- 582 [2] R. Viswanathan, R. Purgert, U. Rao, Materials technology for advanced coal
583 power plants, in: Proc. 1st Int. Conf. ‘Super-High Strength Steels’, Rome, Italy, 2005.
- 584 [3] T. Hamaguchi, H. Okada, S. Kurihara, H. Hirata, M. Yoshizawa, A. Iseda,
585 Microstructural Evaluation of 9Cr-3W-3Co-Nd-B Heat-Resistant Steel (SAVE12AD)
586 After Long-Term Creep Deformation, in: ASME 2017 Pressure Vessels and Piping
587 Conference, American Society of Mechanical Engineers, 2017.
- 588 [4] S. Hollner, E. Piozin, P. Mayr, C. Caës, I. Tournié, A. Pineau, B. Fournier,
589 Characterization of a boron alloyed 9Cr3W3CoVNbBN steel and further improvement

590 of its high-temperature mechanical properties by thermomechanical treatments, *J. Nucl.*
591 *Mater.* 441 (2013) 15–23.

592 [5] D.J. Allen, An investigation of the factors determining creep strength and
593 ductility in Grade 92 steel, in: Kern, T. (ed.) 4th International ECCC Creep & Fracture
594 Conference (ECCC 2017), Dusseldorf, 10-14th September. Dusseldorf: Steel Institute
595 VDEh.

596 [6] P. Yan, Z. Liu, H. Bao, Y. Weng, W. Liu, Effect of tempering temperature on
597 the toughness of 9Cr–3W–3Co martensitic heat resistant steel, *Mater. Des.* 54 (2014)
598 874–879.

599 [7] F. Masuyama, M. Matsui, N. Komai, Creep rupture behavior of advanced 9-12%
600 Cr steel weldment, *Key Eng. Mater.* 171 (1999) 99–108.

601 [8] V. Sklenička, K. Kuchařová, M. Svobodová, M. Kvapilová, P. Král, L. Horváth,
602 Creep properties in similar weld joint of a thick-walled P92 steel pipe, *Mater. Charact.*
603 119 (2016) 1–12.

604 [9] H.J. Schuller, L. Hagn, A. Woitscheck, Cracking in the Weld Region of Shaped
605 Components in Hot Steam Pipe Lines–Materials Investigations, *Der Maschinenschaden.*
606 47 (1974) 1–13.

607 [10] D.J. Abson, J.S. Rothwell, Review of type IV cracking of weldments in 9-12%
608 Cr creep strength enhanced ferritic steels, *Int. Mater. Rev.* 58 (2013) 437–473.

609 [11] J.A. Francis, W. Mazur, H. Bhadeshia, Review Type IV cracking in ferritic
610 power plant steels, *Mater. Sci. Technol.* 22 (2006) 1387–1395.

611 [12] J.D. Parker, Creep cavitation in CSEF steels, in: *Proc. Seventh Int. Conf. Adv.*
612 *Mater. Technol. Foss. Power Plant*, 2013: p. 714.

- 613 [13] Y. Gu, Microstructural investigation of creep behaviour in Grade 92 power plant
614 steels, Ph.D. thesis, 2017.
- 615 [14] Y. Liu, S. Tsukamoto, T. Shirane, F. Abe, Formation Mechanism of Type IV
616 Failure in High Cr Ferritic Heat-Resistant Steel-Welded Joint, *Metall. Mater. Trans. A.*
617 44 (2013) 4626–4633.
- 618 [15] K. Kimura, Y. Takahashi, Evaluation of long-term creep strength of ASME
619 Grades 91, 92, and 122 type steels, in: *ASME 2012 Press. Vessel. Pip. Conf.*, American
620 Society of Mechanical Engineers, 2012: pp. 309–316.
- 621 [16] M.S. L. Havelka, P. Mohyla, Thermal cycle measurement of P92 welded joints,
622 in: *Proc. 23rd Int. Conf. Met. Mater.*, 2014.
- 623 [17] A.H. Yaghi, D.W.J. Tanner, T.H. Hyde, A.A. Becker, W. Sun, Abaqus Thermal
624 Analysis of the Fusion Welding of a P92 Steel Pipe, in: *SIMULIA Cust. Conf.*, 2011:
625 pp. 622–638.
- 626 [18] A.H. Yaghi, T.H. Hyde, A.A. Becker, W. Sun, Finite element simulation of
627 welding and residual stresses in a P91 steel pipe incorporating solid-state phase
628 transformation and post-weld heat treatment, *J. Strain Anal. Eng. Des.* 43 (2008) 275–
629 293.
- 630 [19] X. Xu, G.D. West, J.A. Siefert, J.D. Parker, R.C. Thomson, Microstructural
631 Characterization of the Heat-Affected Zones in Grade 92 Steel Welds: Double-Pass and
632 Multipass Welds, *Metall. Mater. Trans. A.* 49 (2018) 1211–1230.
- 633 [20] X. Xu, G.D. West, J.A. Siefert, J.D. Parker, R.C. Thomson, The Influence of
634 Thermal Cycles on the Microstructure of Grade 92 Steel, *Metall. Mater. Trans. A.* 48
635 (2017) 5396–5414.

636 [21] J. Guo, X. Xu, M.A.E. Jepson, R.C. Thomson, Influence of weld thermal cycle
637 and post weld heat treatment on the microstructure of MarBN steel, *Int. J. Pres. Ves.*
638 *Pip.* 174 (2019) 13-24.

639 [22] A. Benaarbia, X. Xu, W. Sun, A.A. Becker, M.A.E. Jepson, Investigation of
640 short-term creep deformation mechanisms in MarBN steel at elevated temperatures,
641 *Mater. Sci. Eng. A.* 734 (2018) 491-505.

642 [23] L. Li, R. MacLachlan, M. a. E. Jepson, R. Thomson, Microstructural Evolution
643 of Boron Nitride Particles in Advanced 9Cr Power Plant Steels, *Metall. Mater. Trans.*
644 *A.* 44 (2013) 3411–3418.

645 [24] L.A. Giannuzzi, B.W. Kempshall, S.M. Schwarz, J.K. Lomness, B.I. Prenitzer,
646 F.A. Stevie, FIB Lift-Out Specimen Preparation Techniques, in: L.A. Giannuzzi, F.A.
647 Stevie (Eds.), *Introd. to Focus. Ion Beams Instrumentation, Theory, Tech. Pract.*,
648 Springer US, Boston, MA, 2005: pp. 201–228.

649 [25] Y. Li, K. Li, Z. Cai, J. Pan, X. Liu, P. Wang, Alloy design of welding filler
650 metal for 9Cr/2.25 Cr dissimilar welded joint and mechanical properties investigation,
651 *Weld. World.* 62 (2018) 1137–1151.

652 [26] F. Abe, M. Tabuchi, S. Tsukamoto, Metallurgy of Type IV fracture in advanced
653 ferritic power plant steels, *Mater. High Temp.* 28 (2011) 85–94.

654 [27] H. Kitahara, R. Ueji, N. Tsuji, Y. Minamino, Crystallographic features of lath
655 martensite in low-carbon steel, *Acta Mater.* 54 (2006) 1279–1288.

656 [28] N. Nakada, T. Tsuchiyama, S. Takaki, D. Ponge, D. Raabe, Transition from
657 diffusive to displacive austenite reversion in low-alloy steel, *Isij Int.* 53 (2013) 2275–
658 2277.

659 [29] C.L. Briant, S.K. Banerji, Intergranular failure in steel: the role of grain-
660 boundary composition, *Int. Met. Rev.* 23 (1978) 164–199.

661 [30] J. Lin, Y. Liu, T.A. Dean, A review on damage mechanisms, models and
662 calibration methods under various deformation conditions, *Int. J. Damage Mech.* 14
663 (2005) 299–319.

664 [31] T. Sakhivel, M. Vasudevan, K. Laha, P. Parameswaran, K.S. Chandravathi, S.P.
665 Selvi, V. Maduraimuthu, M.D. Mathew, Creep rupture behavior of 9Cr–1.8 W–0.5 Mo–
666 VNb (ASME grade 92) ferritic steel weld joint, *Mater. Sci. Eng. A.* 591 (2014) 111–
667 120.

668 [32] A. Baltusnikas, I. Lukosiute, R. Levinskas, Transformation kinetics of M23C6
669 carbide lattice parameters in low alloyed steel, *Mater. Sci.* 16 (2010) 320–323.

670 [33] F. Abe, Precipitate Design for Creep Strengthening of 9% Cr Tempered
671 Martensitic Steel for Ultra-supercritical Power Plants, *Sci. Technol. Adv. Mater. Sci.*
672 *Technol. Adv. Mater.* 9 (2008) 13002–15.

673 [34] L. Cipolla, H.K. Danielsen, D. Venditti, P.E. Di Nunzio, J. Hald, M.A.J.
674 Somers, Conversion of MX nitrides to Z-phase in a martensitic 12% Cr steel, *Acta*
675 *Mater.* 58 (2010) 669–679.

676 [35] O. Prat, J. Garcia, D. Rojas, G. Sauthoff, G. Inden, The role of Laves phase on
677 microstructure evolution and creep strength of novel 9% Cr heat resistant steels,
678 *Intermetallics.* 32 (2013) 362–372.

679 [36] Z.B. Zhang, O. V Mishin, N.R. Tao, W. Pantleon, Microstructure and annealing
680 behavior of a modified 9Cr–1Mo steel after dynamic plastic deformation to different
681 strains, *J. Nucl. Mater.* 458 (2015) 64–69.

682 [37] M.E. Kassner, T.A. Hayes, Creep cavitation in metals, *Int. J. Plast.* 19 (2003)
683 1715–1748.

684 [38] G. Miyamoto, H. Usuki, Z.-D. Li, T. Furuhashi, Effects of Mn, Si and Cr addition
685 on reverse transformation at 1073 K from spheroidized cementite structure in Fe–0.6
686 mass% C alloy, *Acta Mater.* 58 (2010) 4492–4502.

687 [39] Y.Y. Song, X.Y. Li, L.J. Rong, D.H. Ping, F.X. Yin, Y.Y. Li, Formation of the
688 reversed austenite during intercritical tempering in a Fe–13% Cr–4% Ni–Mo
689 martensitic stainless steel, *Mater. Lett.* 64 (2010) 1411–1414.

690 [40] D. Richardot, J.C. Vaillant, A. Arbab, W. Bendick, *The T92/P92 book*
691 *Vallourec-Mannesmann tubes*, (2000).

692 [41] Y. Song, X. Li, L. Rong, Y. Li, The influence of tempering temperature on the
693 reversed austenite formation and tensile properties in Fe–13% Cr–4% Ni–Mo low
694 carbon martensite stainless steels, *Mater. Sci. Eng. A.* 528 (2011) 4075–4079.

695 [42] N. Nakada, R. Fukagawa, T. Tsuchiyama, S. Takaki, D. Ponge, D. Raabe,
696 Inheritance of dislocations and crystallographic texture during martensitic reversion into
697 austenite, *ISIJ Int.* 53 (2013) 1286–1288.

698